Optics and Lasers in Engineering 172 (2024) 107881

Contents lists available at ScienceDirect

Optics and Lasers in Engineering

journal homepage: www.elsevier.com/locate/optlaseng

OCT-based dynamic mechanical analysis of vitreous humour

Magdalena A. Urbańska [a,*], Sachin S. Thakur [b,c], Sylwia M. Kolenderska [d,e]

[a] School of Food and Advanced Technology, Massey University, Palmerston North, New Zealand
[b] Buchanan Ocular Therapeutics Unit, Department of Ophthalmology, New Zealand National Eye Centre, Faculty of Medical and Health Sciences, University of Auckland, Auckland, New Zealand
[c] School of Pharmacy, Faculty of Medical and Health Sciences, University of Auckland, Auckland, New Zealand
[d] Institute of Physics, Faculty of Physics, Astronomy and Informatics, Nicolaus Copernicus University in Toruń, ul. Grudziądzka 5, Toruń 87-100, Poland
[e] School of Physical and Chemical Sciences, University of Canterbury, Christchurch, New Zealand

ARTICLE INFO

Keywords:
Singular value decomposition
Shear wave
Rayleigh wave
Ocular biomechanics
Velocity dispersion
Viscoelasticity

ABSTRACT

The vitreous humour plays an important role in shock absorption, i.e. the damping of the mechanical movement, to protect the delicate tissues within the eye. However, this damping is different for movements with different frequencies/velocities. While the collective low-frequency (below 100 Hz) damping behaviour of the vitreous humour associated with the saccadic and lens movements is well-studied, to the best of our knowledge, the high-frequency damping behaviour of the vitreous humour, which represents the response of the microstructural components, is not exhaustively documented. Here, we utilise a non-destructive testing method called Optical Coherence Tomography (OCT) to measure the high-frequency (100–350 Hz, waves able to probe approximately 500 μm distances) biomechanical behaviour of the vitreous humour. We parametrise this behaviour by calculating the shear storage modulus, shear loss modulus and phase angle. We compare these parameters to their low-frequency counterparts obtained with a rheometer, providing a comprehensive mechanical spectrum of the vitreous humour behaviour. The processing method developed in this study and the data collected help better understand the vitreous humour shock absorption properties. Consequently, they could allow a development of better vitreous humour substitutes. The local probing of the high-frequency regime and the non-invasive character of the OCT method provide new qualities in mapping the damping behaviour.

1. Introduction

The vitreous humour is a gel substance occupying the interior cavity of the eye. Among its many roles, the vitreous humour has an important function in absorbing shocks during eye movements thereby protecting delicate intraocular tissues [1]. Mechanically, the vitreous humour is a shear-thickening non-Newtonian biofluid [2]. Therefore, the sample is expected to express high damping behaviour for a high frequency of shear movement. It was previously observed that between 0.1 and 5 Hz, the elastic behaviour of the vitreous humour is dominant over the viscous behaviour [3–6]. Above that frequency range, the viscous behaviour becomes more dominant and increases with frequency. Such high damping of the vitreous humour is critical during fast eye movements, such as in high-impact falls or collisions. If not mitigated, such movements, especially shear movements, may lead to vitreous or even retinal detachment [7,8]. These observations provide great insight into the working of vitreous humour and help design its synthetic substitutes [9,7,8]. However, the methods used to obtain them are destructive and limited to frequencies under 100 Hz, due to the limitation of commercial rheometers, making the information about the vitreous humour behaviour incomplete and not obtainable in a clinical setting.

Increasing the frequency of the measurement not only provides information about fast behaviour of the sample but also, due to probing smaller areas in the sample, reflects the microstructural behaviour in contrast to the collective behaviour [10]. Such high-frequency local probing is challenging due to higher damping behaviour and faster, local acquisition requirement. Nonetheless, several research methods were developed for assessing high-frequency viscoelastic behaviour, such as optically local probe oscillations [11], velocimetry [12], or Magnetic Resonance Elastography [13]. Unfortunately, we have found only two studies of the vitreous humour that explored frequencies above 100 Hz: 110 Hz [14] and 1200 Hz [13]. The latter study reported excessively high shear moduli which could be caused by compression in the measurement that exceeded the linear regime. Because of this discrepancy as

* Corresponding author.
E-mail address: murb435@aucklanduni.ac.nz (M.A. Urbańska).

https://doi.org/10.1016/j.optlaseng.2023.107881
Received 2 March 2023; Received in revised form 25 September 2023; Accepted 26 September 2023
Available online 7 October 2023

well as a limited number of frequencies measured, these two studies are insufficient to provide information about the general high-frequency behaviour, assess fast dynamics and local-scale microstructure [10, 15]. Our previous article [16] described the high-frequency damping behaviour of a vitreous humour phantom over a broad frequency range. The vitreous humour phantom reached an almost purely viscous state (high damping) for high frequencies (~300 Hz); similar behaviour is expected for the vitreous humour.

To determine the high-frequency behaviour of the vitreous humour, we build on the method we developed for analysing such behaviour in a vitreous humour phantom [16]. This method induces surface waves in the sample and detects its propagation at micro- to nanoscale within the sample's surface with an Optical Coherence Tomography (OCT) system. The surface waves' velocity and attenuation are used to determine the sample's mechanical properties at high frequencies (above 100 Hz). This method is less invasive than a rheometer measurement, hence better preserving the hyaluronic acid-collagen network of the vitreous humour intrinsically connected to its mechanical properties.

The application of this method to the vitreous humour is challenging because, unlike the phantoms, we cannot control the viscous properties and the surface shape of the vitreous humour, which causes the compressional wave to dominate and overlap the weak surface wave in the recorded signal. Therefore, it is impossible to separate these waves due to highly different velocities by recording over a longer distance between the wave's source and detection, as done for the phantoms. Another way is to separate these waves in post-processing. However, current post-processing methods [17–19], such as directional-spatial filters, can be challenging with overlapping waves and require providing a spatial frequency limit. This is why we decided to develop a new method, which implements Singular Value Decomposition (SVD) to separate spatiotemporal signals into sub-components with unique spatial distributions. This method is widely used in ultrasound image decluttering [20], Doppler ultrasound imaging [21], and motion-artefacts removal in 2D real-time OCT imaging [22].

Here, we propose using SVD to identify the compressional wave component in the spatiotemporal data and remove it. We induce high-frequency mechanical waves *in vitro* vitreous humour samples and register their propagation over a small distance with OCT. Then, we use the SVD-based compressional-wave-removal method to obtain surface wave propagation parameters and calculate the mechanical properties of the vitreous humour. To produce a complete mechanical spectrum, rheometer measurements are also performed, and its results are analysed.

2. Materials and methods

2.1. Sample preparation

In our measurements, extracted porcine vitreous humour samples are used. Six "fresh", unscalded porcine eyes were obtained from a butcher immediately after extraction. A clear crystalline lens indicated a short post-mortem time [23]. Three were measured with an OCT system and three with a rheometer. After the eye extraction from the eye socket, the eyes were kept in a solution of common salt (NaCl, 7 g) in water (800 ml) at 36 °C for the OCT measurement. For the rheological study, eyes were kept moisturised instead at 25 °C. Each vitreous was carefully extracted from the eye before the measurement and placed in a petri dish. The extraction process took about 10–15 min. Due to the inhomogeneous nature of the vitreous humour [24], the crystalline lens was left attached for OCT measurement to serve as a location reference within the vitreous humour and, for consistency, the measurements were only performed at a short distance from the lens (Fig. 1). The measurements were performed shortly after extraction when the extracted vitreous humour is expected to be close to the steady state [25] and no visual change was observed during the measurement. During the OCT measurement, the vitreous humour was cooled down to ambient temperature (21 °C); the rheometer measurement was kept at 25 °C.

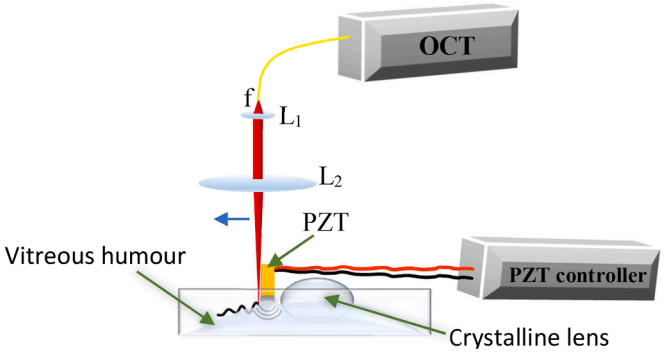

Fig. 1. A schematic of the measurement setup with the extracted porcine vitreous humour. PZT -piezoelectric transducer, OCT – Optical Coherence Tomography system, L_1 – collimating lens, L_2 – focusing lens, f – fibre output.

2.2. System and data acquisition

2.2.1. Rheometer

Rheological data are obtained with an oscillatory frequency sweep test using a controlled-stress rheometer (TA Instruments, Model HR-2) with a 1 mm gap between smooth, parallel plates of 40 mm diameter. For this measurement, the sample is inserted between the plates where the bottom plate is stationary, and a fixed small angle rotates the upper plate with increasing frequency (0.1–16 Hz). The chosen fixed angle for this measurement corresponded to 3% strain (the upper limit of the linear regime [26]).

2.2.2. OCT system

The system consisting of a custom-made Spectral-domain optical coherence tomography (SD-OCT) setup (wave detection) and a piezoelectric transducer (wave excitation, (PK4DLP1, Thorlabs)) described in detail in [16] was used for these experiments. The SD-OCT system consists of a broadband light source (SLD, Superlum Broadlighter T840, 780-920 nm) and spectrometer (1200 lines/mm diffraction grating and a camera with a 70 kHz rate (spL8192–70 km, Basler)), providing the axial resolution of ~4 μm and the imaging depth of ~1.5 mm. The piezoelectric transducer was supplied with a 0.2 ms long square pulse, providing maximum displacement below 3 μm deep (about 0.06% strain), which is below the 1% strain and within the linear viscoelastic regime.

2000 M-scans (1D motion scans, each consisting of 7000 spectra, corresponding in total to 28 ms) were acquired every 50 μm in the area close to the lens, over 0.5–0.75 mm depending on the curvature of the extracted vitreous humour surface. The excitation was induced during recording at 1 ms (70 M-scan). These first 70 M-scans were removed in further analysis.

2.3. Compressional wave removal

The process of obtaining the displacement graph (movement of the waves with time and distance on the sample, Fig. 2a–c) from our previous article was followed, i.e. collected spectra were Fourier transformed, and the movement of the sample surface due to the waves propagation was extracted from the phase changes at the surface position. Previously, we removed the compressional wave from the displacement graph by separating the surface wave and the compressional wave in time (recording further from the source of the wave). However, for the vitreous humour, such a setting was challenging due to a dominating compressional wave, high surface wave attenuation, and uneven surface.

Displacement graphs for three vitreous humour samples are shown in

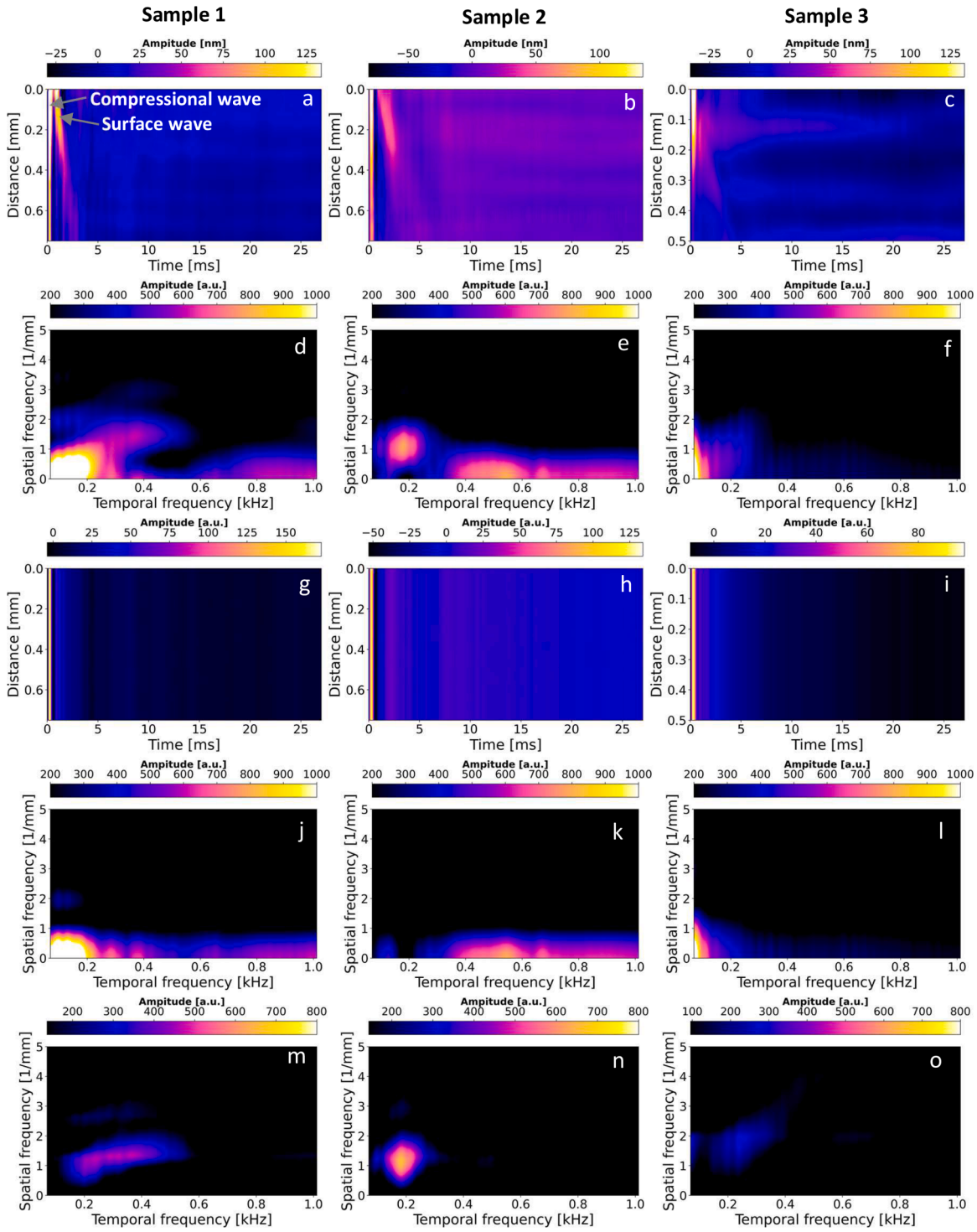

Fig. 2. Steps used to obtain the dispersion and attenuation graphs without the compression wave component for 3 different vitreous humour samples. Displacement graphs (a–c) obtained during OCT measurement and corresponding to them dispersion graphs (d–f). Displacement graphs were extracted using SVD with components corresponding to the compressional wave (g–i) and corresponding dispersion graphs (j–l). The final graphs with the surface wave information (m–o) were generated by subtracting the dispersion graphs corresponding to the compressional wave (j–l) from the raw dispersion graphs (d–f).

Fig. 2a–c. Each of these displacement graphs has a somewhat weaker surface wave caused by slightly different distances between the source and detector, surface irregularities and biological variations in the mechanical properties of these samples. These vitreous humour samples represent a different level of difficulty in separating the surface wave from the compressional wave, with Fig. 2a being the least and Fig. 2c being the most challenging.

To help minimise the effect of the compressional wave in such data, we propose a method based on SVD. This method decomposes spatio-temporal information into individual singular vectors and allows grouping them into unique spatiotemporal components (frames). The SVD process of separating individual spatiotemporal frames presented in [27] was used to extract the propagation of the compressional wave. The inputs of the SVD algorithm were displacement graphs consisting of

1930 time-points and 10–15 space-points, i.e. 1D temporal data changed over the propagation of the wave with space, creating a 2D spatiotemporal graph. This 2D data was decomposed into singular vectors. Those vectors are correlated one with another and set in a temporal order to provide a similarity matrix (Fig. 3). Two frames with unique spatial trends could be identified in the similarity matrix (yellow squares in the similarity matrix, Fig. 3), below and above 11 time-point (1 time-point corresponds to 0.014 ms). Within the first frame (below 11 time-point), another subspace below 2 time-points was observed (orange square). This small subspace consists of singular vectors, which create a displacement graph with two waves identified as surface and compressional waves. Singular vectors from 3rd to 11th time-point combine the information of the compressional wave and another wave which could not be identified. In the displacement graph created with singular vectors above 11 time-point (from 12 to 1930 time-points, Fig. 3), only the compressional wave was evident.

Interestingly, extracting only a surface wave from the similarity matrix was impossible. This could be due to insufficient resolution in time, as surface wave information is the slowest component of the spatiotemporal data and seems to be present below the time resolution of the measurement (below 1 time-point). As a result, the compressional wave was extracted and removed. To ensure that only spatiotemporal information corresponding to the compressional wave is present, the singular vectors above 200 time-point were chosen as purely corresponding to the compressional wave (from 200 to 1930 time-points, Fig. 3).

The displacement graphs generated based on the singular vectors above 200 time-point for these samples (Fig. 2g–i), as well as the displacement graphs with both surface and compressional wave (Fig. 2a–c), were zero-padded to 4096 in both dimensions and Fourier transformed. The amplitude of the transform was taken using absolute value. As a result, two dispersion graphs were created for each sample, one corresponding to the compressional wave (Fig. 2j–l) and the other to the surface and compressional waves (Fig. 2d–f). These graphs were subtracted to obtain the dispersion graphs corresponding to the surface wave (Fig. 2m–o). Any remaining artefacts in the dispersion graphs were removed using a horizontal line filter (by estimating distortion frequency as spectral peak in the vertical dimension and removing it with a frequency filter). From the phase of the Fourier Transform, attenuation graphs were generated, and the procedure was repeated.

2.4. Mechanical properties estimation

On the dispersion and attenuation graphs, the spatial (k) and temporal (f) frequencies corresponding to the maximum amplitudes were determined. These frequencies were used to calculate the velocity (c_{surf}) and attenuation (α_{surf}) of the surface wave, as per the equation:

$$c_{surf} = \frac{f}{k'}, \quad \alpha_{surf} = -k'' \tag{1}$$

Additionally, for each found maximum amplitude, a Gaussian fit was used for each line of the dispersion graphs to obtain an uncertainty of the maximum position and hence the error for the velocity value. The extracted surface wave velocity and attenuation values were recalculated to the shear wave velocity (c_{sh}) and attenuation (c_{sh}) using an antisymmetric Lamb wave dispersion equation [16].

These values were compared to the velocity and attenuation of the shear wave calculated using shear storage (G') and loss (G'') moduli from the oscillatory rheometer test, as follows:

$$c_{sh} = \sqrt{\frac{2\frac{\sqrt{(G'^2+G''^2)}}{\rho}}{1+\frac{G'}{\sqrt{(G'^2+G''^2)}}}}, \tag{2}$$

$$\alpha_{sh} = f_{rheo}\sqrt{\frac{0.5\rho}{\sqrt{(G'^2+G''^2)}}\left(1-\frac{G'}{\sqrt{(G'^2+G''^2)}}\right)} \tag{3}$$

After comparing the velocities and attenuations of the shear wave over the wide frequency range, we have compared the main mechanical parameters that allow us to describe the sample behaviour, such as shear storage modulus, shear loss modulus and the phase angle. The storage modulus represents the stored energy, and the shear loss modulus represents the lost energy of the sample in motion. The phase angle, also called the phase shift, is an indicator of the relation between viscous and elastic properties of a material. For an ideal viscous flow, a phase angle will be 90°, as the storage modulus will be equal to 0. For an ideal solid (purely elastic deformation), a 0° phase angle will be obtained, as the loss modulus will be equal to 0 [28]. While storage and loss moduli are obtained directly in the rheometer measurements, in the OCT measurements they are calculated based on shear wave velocity and

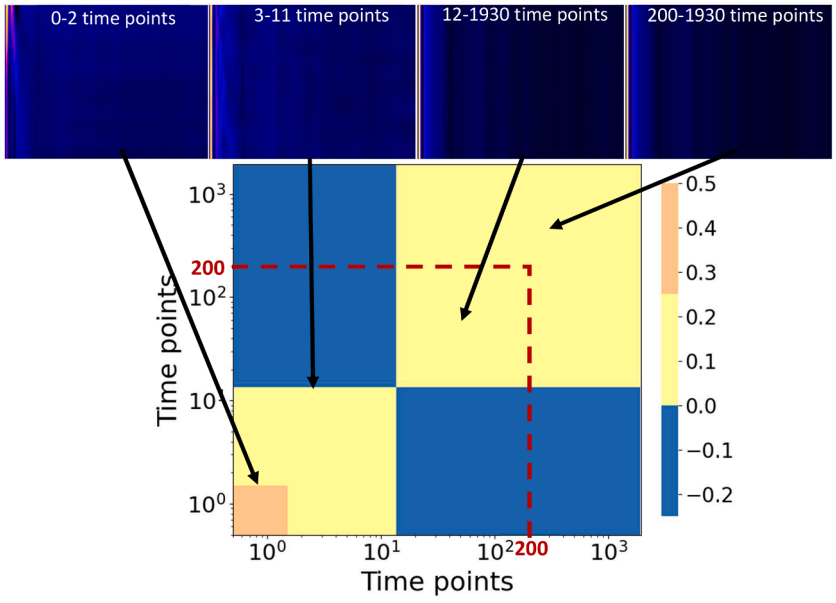

Fig. 3. Spatial similarity matrix with discrete colour scale and logarithmic x and y scales. Each group of correlated spatial vectors is represented as a square. Data corresponding to each group of singular vectors is displayed in the form of displacement graphs above the spatial similarity matrix.

attenuation values using the following formulae:

$$G'(f) = \rho c_{sh}^2(f) \frac{1 - \left(\frac{\alpha_{sh}(f)}{f}\right)^2 c_{sh}^2(f)}{\left(1 + \left(\frac{\alpha_{sh}(f)}{f}\right)^2 c_{sh}^2(f)\right)^2} \quad (4)$$

$$G''(f) = \frac{2\rho \left(\frac{\alpha_{sh}(f)}{f}\right) c_{sh}^3(f)}{\left(1 + \left(\frac{\alpha_{sh}(f)}{f}\right)^2 c_{sh}^2(f)\right)^2} \quad (5)$$

Finally, we observe the changes in the response of our samples with frequency by calculating the phase angle between elastic and viscous response using the moduli obtained with rheometer and OCT in the following way:

$$\delta = \arctan\left(\frac{G''}{G'}\right) \quad (6)$$

3. Results and discussion

Fig. 4 presents the dispersion and attenuation graphs for three vitreous humour samples. The maximum amplitude is indicated on each graph with a light blue marker. Only maxima which could be found in both the dispersion and attenuation graphs were marked. The extracted velocity and attenuation values are presented in Fig. 5a and Fig. 5b, respectively. The parameters calculated based on these values, shear storage modulus, shear loss modulus and the phase angle, are compared with the rheometer data in Fig. 5c and Fig. 5d, respectively.

It can be seen that the shear wave velocity (Fig. 5a) gradually increases with frequency up to about 5 Hz when a rapid rate of this increase is observed. The rate of the change of the velocity with frequency exponentially decreases from 1700 mm to 5.5 mm with a rapid drop up to 0.1 Hz, and a slow decrease above 5 Hz. In the high-frequency regime (100-350 Hz) this rate stays approximately constant with values varying between 500 and 800 μm. Attenuation expresses a similar trend to velocity, but it is nearly negligible below 5 Hz. This trend suggests that for the vitreous humour, as expected, a shear wave has a higher velocity and is more attenuated at high frequencies.

Fig. 5c shows that initially, in frequencies below 0.1 Hz, the shear storage and loss moduli are increasing and decreasing, respectively. This behaviour can also be observed in the phase angle (Fig. 5d, decrease of the phase angle), suggesting a decrease in the damping behaviour. Between 0.1 and 1 Hz, the vitreous humour behaviour is rather constant and has a significant elastic component (storage modulus is higher than loss modulus). This dominant elastic behaviour for 0.1–1 kHz (0.6–6 rad/sec) was previously observed by a number of researchers with values for the storage modulus (0.2–6 Pa) and the loss modulus (0.1 - 1 Pa) comparable to this study, but slightly lower phase angle, estimated based on these moduli (3–22°) [25,29,30].

In the 0.1–1 Hz frequency range, the lower viscosity allows the lens to change the focus of the eye swiftly [2]. When frequency reaches about 1 Hz, an upturn in the viscous behaviour is observed (as evidenced by the increase in the phase angle, Fig. 5d). At about 5 Hz, the viscous behaviour starts to dominate (phase angle higher than 45°). It was previously shown that human depth perception decreases from contrast disparities (stripes with different contrast characteristics) oscillating at around 1 Hz and from a geometric disparity (stripes with different geometric characteristics) oscillating above 5 Hz [31], which could be related to the observed increase in the damping behaviour of the vitreous humour. Further increase in the viscous behaviour with frequency can be associated with the damping of the oscillation caused by the saccadic eye movements (about 20 Hz [32]). Above 150 Hz, the shear storage modulus seems to be approximately constant or even slightly decreasing, but the shear loss modulus increases up to 5 times. This behaviour can also be observed in phase angle, which almost reaches a purely viscous state. It was previously stated that in this high-frequency region, the vibrational eigenfrequencies are present [33]. The vibrational radial modes of an eyeball were modelled to be 67 ± 10 Hz, 186 ± 24 Hz, 307 ± 45 Hz [33]. In another study, the resonant frequency modes of the eyeball were also shown to increase with the intraocular pressure [34] and for some pressures above 25 mmHg increased above 100 Hz (limit of the rheometric measurement). This shows the relevance of the values measured in the high-frequency region.

The behaviour of the vitreous humour is similar to the one presented for a vitreous humour phantom at high frequency (100-300 Hz), with the shear storage moduli slightly decreasing and the shear loss modulus rapidly increasing. However, at a lower frequency (0.1–1 Hz), when the phase angle is approximately constant for the vitreous humour, the

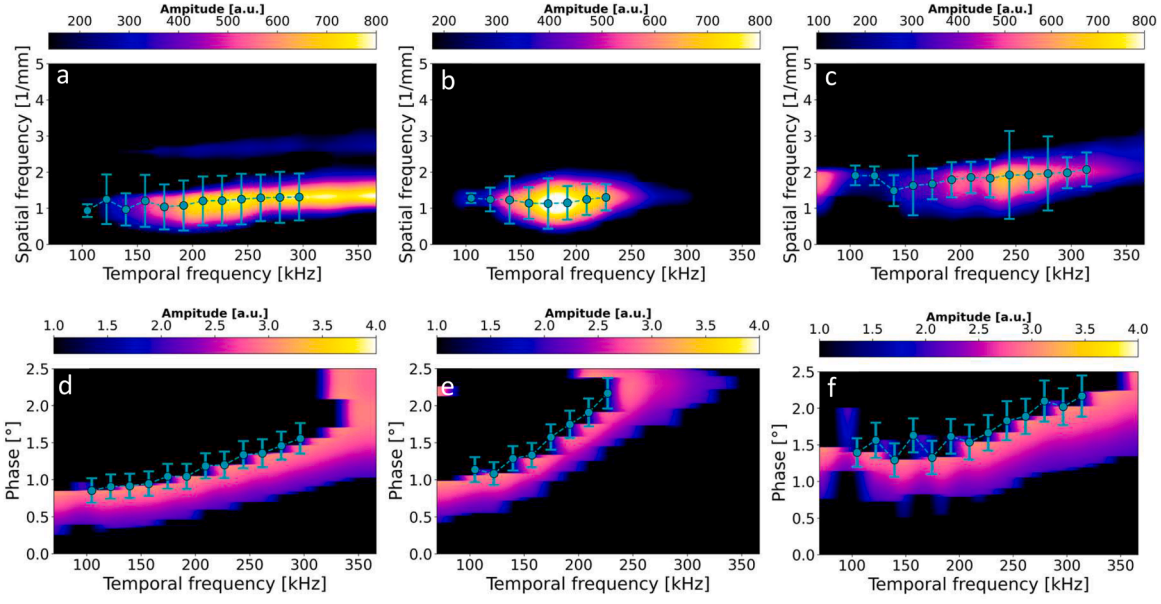

Fig. 4. Dispersion (a–c) and attenuation (d–f) graphs, obtained from the method presented in Fig. 2, with found maxima for samples 1(a,d), 2(b,e) and 3(c,f) marked with light blue markers.

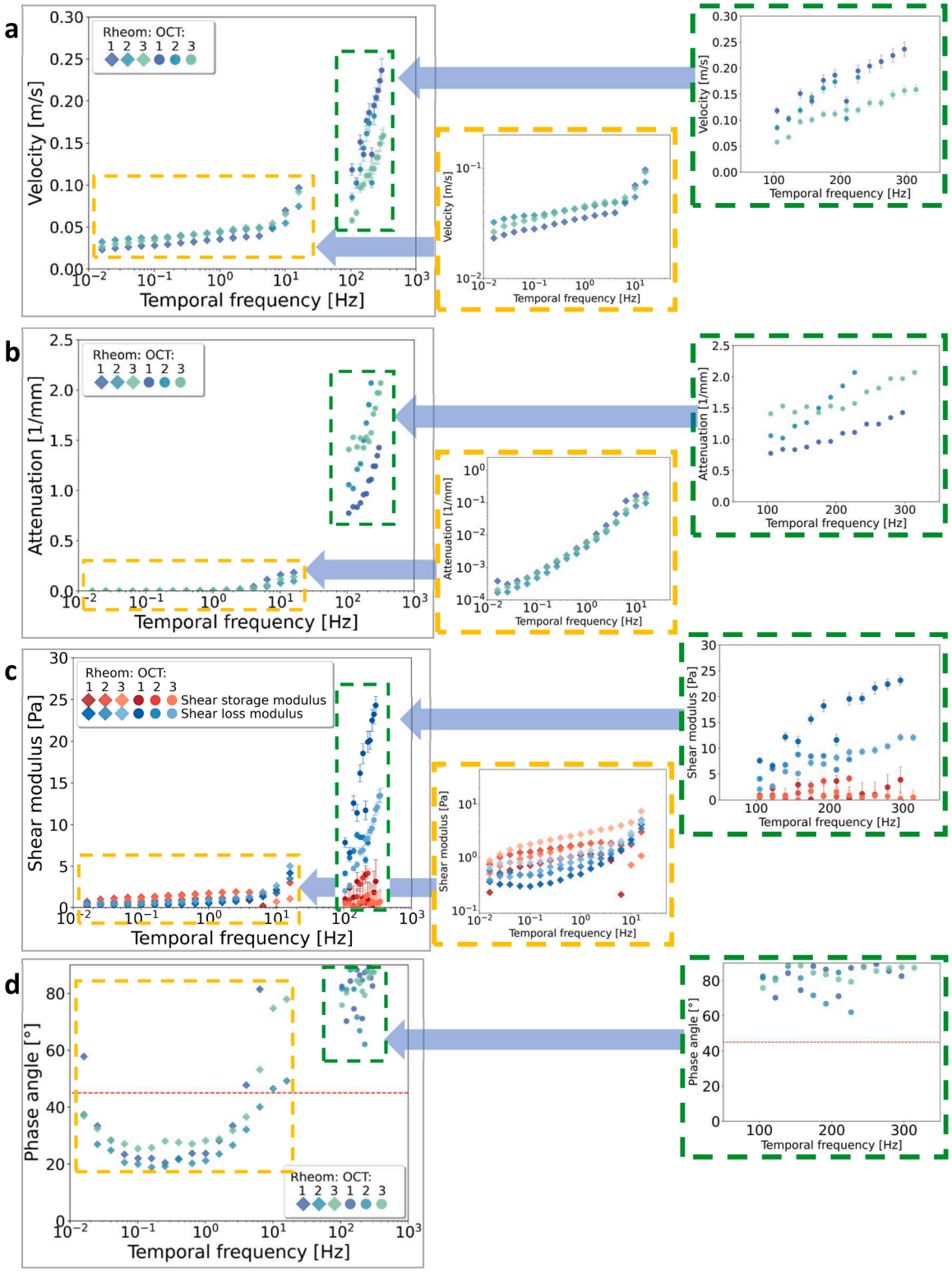

Fig. 5. Parameters obtained for 3 vitreous humour samples studied with an OCT system (OCT) and 3 other vitreous humour samples measured with the rheometer (Rheom). Velocity (a, OCT) and attenuation (b, OCT) of a shear wave calculated using an antisymmetric Lamb wave dispersion equation with the spatial and temporal frequencies extracted from dispersion and attenuation graphs. Velocity (a, Rheom) and attenuation (b, Rheom) of a shear wave calculated using shear storage and loss moduli obtained with the rheometer. Shear storage and loss moduli calculated based on the shear wave velocity and attenuation (c, OCT) and shear storage and loss moduli obtained using a rheometer (c, Rheom). Phase angle calculated based on the shear storage and loss moduli for the OCT system (d, OCT) and rheometer (d, Rheom).

phase angle for the vitreous humour phantom increases. This study focused on using the OCT-based technique for frequencies above 100 Hz. However, further analysis of frequencies under 100 Hz could be achieved using a longer excitation pulse or individual sinusoidal waves. The OCT-based local probing has the potential to be extended over a much bigger area using B-scan or even C-scan acquisition and provide information about microstructural differences and changes within the vitreous humour and has the capacity to be developed towards *in vivo* application. Additionally, it could be used to monitor the change in the vitreous humour biomechanical properties with natural age-related degeneration of tissue due to liquefaction and aggregation of the collagen fibrils [1,35]. The age-related degeneration could be accelerated by different ocular diseases such as diabetic retinopathy (DR) [36, 37], age-related macular degeneration (AMD) [38] or glaucoma [39, 40]. Due to the liquefaction of the vitreous humour, there is a separation of the liquid and gel phases of the vitreous humour which differ in mechanical properties [3,6,29]. Since the OCT-based method allows for the detection of local properties it can be used to measure both the gel and liquid phase of vitreous humour without physically separating them.

4. Conclusion

We have demonstrated that by using SVD on the spatiotemporal data, we can eliminate the influence of the compressional wave on the extraction of the mechanical properties of the vitreous humour. We have shown that the vitreous humour damping behaviour (expressed with the loss modulus) continues to grow in the 150–350 Hz frequency range. The sample reaches almost purely viscous behaviour (90° phase angle), which is highly different from its low-frequency behaviour. The novel method presented in this work will allow the non-destructive analysis of broad frequency biomechanical changes caused by pathogenic, age-related, and natural biological variations, which can lead to new diagnostic tools.

Funding

This work was supported by Dodd-Walls Centre and the University of Auckland's internal research and maintenance funds.

CRediT authorship contribution statement

Magdalena A. Urbańska: Conceptualization, Methodology, Investigation, Data curation, Software, Formal analysis, Writing – original draft, Visualization. **Sachin S. Thakur:** Investigation, Data curation, Writing – review & editing. **Sylwia M. Kolenderska:** Writing – review & editing.

Declaration of Competing Interest

The authors declare that they have no known competing financial interests or personal relationships that could have appeared to influence the work reported in this paper.

Data availability

Data will be made available on request.

Acknowledgements

The authors would like to acknowledge Dr. Jami Shepherd (Johnson) for introducing us to the concept of singular value decomposition and the Marsden Fund managed by Royal Society Te Apārangi for making the experimental work possible. We would also like to thank "Buchanan Ocular Therapeutics Unit, Department of Ophthalmology, University of Auckland" for providing us with the rheometry data and Prof. Frédérique Vanholsbeeck for providing access to the lab and all the necessary equipment.

References

[1] Sebag J. Vitreous: in health and disease. Vitreous: in health and disease. Springer; 2014. https://doi.org/10.1007/978-1-4939-1086-1.
[2] Silva AF, Alves MA, Oliveira MSN. Rheological behaviour of vitreous humour. Rheol Acta 2017;56:377–86.
[3] Schulz A, Wahl S, Rickmann A, Ludwig J, Stanzel BV, von Briesen H, Szurman P. Age-related loss of human vitreal viscoelasticity. Transl Vis Sci Technol 2019;8(3): 56. -56.
[4] Watts F, Tan LE, Wilson CG, Girkin JM, Tassieri M, Wright AJ. Investigating the micro-rheology of the vitreous humor using an optically trapped local probe. J Opt 2013;16(1):015301.
[5] Shafaie S, Hutter V, Brown MB, Cook MT, Chau DY. Diffusion through the *ex vivo* vitreal body–bovine, porcine, and ovine models are poor surrogates for the human vitreous. Int J Pharm 2018;550(1–2):207–15.
[6] Filas BA, Zhang Q, Okamoto RJ, Shui YB, Beebe DC. Enzymatic degradation identifies components responsible for the structural properties of the vitreous body. Investig Ophthalmol Visual Sci 2014;55(1):55–63.
[7] Angunawela RI, Azarbadegan A, Aylward GW, Eames I. Intraocular fluid dynamics and retinal shear stress after vitrectomy and gas tamponade. Investig Ophthalmol Visual Sci 2011;52(10):7046–51.
[8] Semeraro F, Morescalchi F, Russo A, Romano MR, Costagliola C. Tamponade or filling effect: changes of forces in myopic eyes. BioMed Res Int 2014:2014.
[9] Kleinberg TT, Tzekov RT, Stein L, Ravi N, Kaushal S. Vitreous substitutes: a comprehensive review. Surv Ophthalmol 2011;56:300–23.
[10] Schroyen B, Vlassopoulos D, Van Puyvelde P, Vermant J. Bulk rheometry at high frequencies: a review of experimental approaches. Rheol Acta 2020;59(1):1–22.
[11] Pokki J, Ergeneman O, Sevim S, Enzmann V, Torun H, Nelson BJ. Measuring localized viscoelasticity of the vitreous body using intraocular microprobes. Biomed Microdev 2015;17:1–9.
[12] Rossi T, Querzoli G, Pasqualitto G, Iossa M, Placentino L, Repetto R, Ripandelli G. Ultrasound imaging velocimetry of the human vitreous. Exp Eye Res 2012;99: 98–104.
[13] Clayton EH, Wang Q, Song SK, Okamoto RJ, Bayly PV. Magnetic resonance elastography of the mouse vitreous humor *in vivo*. In: Proceedings of the conference proceedings of the society for experimental mechanics series. 4. New York, NY: Springer; 2012. p. 129–33.
[14] Bettelheim FA, Wang TJY. Dynamic viscoelastic properties of bovine vitreous. Exp Eye Res 1976;23:435–41.
[15] Fritz G, Pechhold W, Willenbacher N, Wagner NJ. Characterising complex fluids with high frequency rheology using torsional resonators at multiple frequencies. J Rheol 2003;47(2):303–19.
[16] Urbańska MA, Kolenderska SM, Rodrigues SA, Thakur SS, Vanholsbeeck F. Broadband-excitation-based mechanical spectroscopy of highly viscous tissue-mimicking phantoms. Opt Express 2022;30(1):603–18.
[17] Zhao H, Song P, Meixner DD, Kinnick RR, Callstrom MR, Sanchez W, Chen S. External vibration multi-directional ultrasound shearwave elastography (EVMUSE): application in liver fibrosis staging. IEEE Trans Med Imaging 2014;33 (11):2140–8.
[18] Liu HC, Kijanka P, Urban MW. Two-dimensional (2D) dynamic vibration optical coherence elastography (DV-OCE) for evaluating mechanical properties: a potential application in tissue engineering. Biomed Opt Express 2021;12(3): 1217–35.
[19] Mellema DC, Song P, Kinnick RR, Urban MW, Greenleaf JF, Manduca A, Chen S. Probe oscillation shear elastography (PROSE): a high frame-rate method for two-dimensional ultrasound shear wave elastography. IEEE Trans Med Imaging 2016; 35(9):2098–106.
[20] Ledoux LAF, Brands PJ, Hoeks APG. Reduction of the clutter component in Doppler ultrasound signals based on singular value decomposition: a simulation study. Ultrason Imaging 1997;19:1–18.
[21] Baranger J, et al. Adaptive spatiotemporal SVD clutter filtering for ultrafast doppler imaging using similarity of spatial singular vectors. IEEE Trans Med Imaging 2018;37:1574–86.
[22] Scholler, J. Motion artifact removal and signal enhancement to achieve *in vivo* dynamic full field OCT. (2019) doi:10.1364/OE.27.019562.
[23] Ojo OM, Ajayi OB, Musa MJ. Spectral transmission of porcine crystalline lens at post-mortem interval. J Niger Optom Assoc 2020;22(1):35–43.
[24] Lee B, Litt M, Buchsbaum G. Rheology of the vitreous body. Part I: viscoelasticity of human vitreous. Biorheology 1992;29(5–6):521–33.
[25] Nickerson CS, Park J, Kornfield JA, Karageozian H. Rheological properties of the vitreous and the role of hyaluronic acid. J Biomech 2008;41(9):1840–6.
[26] Nickerson CS. Engineering the mechanical properties of ocular tissues - CaltechTHESIS. California Institute of Technology; 2006.
[27] Baranger J, Arnal B, Perren F, Baud O, Tanter M, Demené C. Adaptive spatiotemporal SVD clutter filtering for ultrafast Doppler imaging using similarity of spatial singular vectors. IEEE Trans Med Imaging 2018;37(7):1574–86.
[28] Mezger T. The rheology handbook: for users of rotational and oscillatory rheometers. European Coatings; 2020.
[29] Tram NK, Swindle-Reilly KE. Rheological properties and age-related changes of the human vitreous humor. Front Bioeng Biotechnol 2018;6:199.

[30] Sharif-Kashani P, Hubschman JP, Sassoon D, Kavehpour HP. Rheology of the vitreous gel: effects of macromolecule organization on the viscoelastic properties. J Biomech 2011;44(3):419–23.
[31] Dobias JJ, Stine WW. Temporal dynamics of the Venetian blind effect. Vis Res 2012;60:79–94.
[32] Tabernero J, Artal P. Lens oscillations in the human eye. Implications for post-saccadic suppression of vision. PLoS One 2014;9(4):e95764. https://doi.org/10.1371/journal.pone.0095764. Apr 22PMID: 24755771; PMCID: PMC3995773.
[33] Aloy MÁ, Adsuara JE, Cerdá-Durán P, Obergaulinger M, Esteve-Taboada JJ, Ferrer-Blasco T, Montés-Micó R. Estimation of the mechanical properties of the eye through the study of its vibrational modes. PloS One 2017;12(9):e0183892.
[34] Shih PJ, Guo YR. Resonance frequency of fluid-filled and prestressed spherical shell—a model of the human eyeball. J Acoust Soc Am 2016;139(4):1784–92.
[35] Le Goff MM, Bishop PN. Adult vitreous structure and postnatal changes. Eye 2008;22(10):1214–22.
[36] Ono R, Kakehashi A, Yamagami H, Sugi N, Kinoshita N, Saito T, Tamemoto H, Kuroki M, Ishikawa S, Kawakami M. Prospective assessment of proliferative diabetic retinopathy with observations of posterior vitreous detachment. Int Ophthalmol 2005;26:15–9.
[37] Sebag J. Abnormalities of human vitreous structure in diabetes. Graefe's Arch Clin Exp Ophthalmol 1993;231:257–60.
[38] De Smet MD, Gad Elkareem AM, Zwinderman AH. The vitreous, the retinal interface in ocular health and disease. Ophthalmologica 2013;230(4):165–78.
[39] Schwab C, Glatz W, Schmidt B, Lindner E, Oettl K, Riedl R, Wedrich A, Ivastinovic D, Velikay-Parel M, Mossboeck G. Prevalence of posterior vitreous detachment in glaucoma patients and controls. Acta Ophthalmol 2017;95(3):276–80.
[40] Batta P, Engel HM, Shrivastava A, Freeman K, Mian U. Effect of partial posterior vitreous detachment on retinal nerve fiber layer thickness as measured by optical coherence tomography. Arch Ophthalmol 2010;128(6):692–7.

Magdalena Urbańska received her MSc degree in Technical Physics from Nicolaus Copernicus University, Poland, in 2015, and the PhD degree in Physics from the University of Auckland, New Zealand, in 2022. She is a Research Fellow at the Massey University (New Zealand) since 2022. Her research interest includes non-destructive biomedical imaging and biomechanical measurements. Currently, she uses her expertise in these areas to gain insight into biological systems and provide solutions for loses during storage of perishable horticultural products.

Sachin Thakur received his BPharm (Hons) degree from the University of Auckland, New Zealand, in 2010, and his PhD degree in Pharmaceutical Sciences from the University of Queensland, Australia in 2016. He was with the University of Auckland as a Post-doctoral research fellow in 2016, Lecturer in 2019 and has been a Senior Lecturer at this institution since 2022. His-research interests include the development of drug delivery systems as well as in vitro models in which to test their effectiveness. Namely, he has a history in developing such models for ocular drug delivery as well as ultrasound-responsive drug delivery.

Sylwia Kolenderska received her MSc degree in Technical Physics in 2011 and the PhD degree in Physical Sciences in 2015 from Nicolaus Copernicus University, Poland. She was with the University of Auckland (New Zealand) as a Research Fellow from 2016 until early 2021 and currently, is an Assistant Professor at Nicolaus Copernicus University (Poland) and an Adjunct Fellow at the University of Canterbury (New Zealand). She specialises in Optical Coherence Tomography and her research is focused on pushing the limitations of Optical Coherence Tomography imaging in terms of axial resolution, image quality and information content.